Nano Research

Open Access

Research Article

Optimizing the microstructure of high-entropy alloys to achieve efficient hydrogen storage at room temperature

Long Luo[1,2], Kaicong Yu[1], Liangpan Chen[1], Huimin Han[1], Yuan Deng[3,4] ✉, Bingbing Chen[5] ✉, Yong Cheng[6], Yongzhi Li[1,2] ✉, and Xinfang Zhang[1]

[1] *School of Rare Earth Industry, Inner Mongolia University of Science and Technology, Baotou 014010, China*
[2] *Baotou Materials Research Institute of Shanghai Jiao Tong University, Baotou 014010 , China*
[3] *Institute of Modern Physics, Fudan University, Shanghai 200433, China*
[4] *Inner Mongolia Rare Earth Ovonic Metal Hydride Co., Ltd., Baotou 014010, China*
[5] *Department of Energy Science and Engineering, Nanjing Tech University, Nanjing 211816, China*
[6] *State Key Laboratory of Rare Earth Resource Utilization, Changchun Institute of Applied Chemistry, Chinese Academy of Sciences, Changchun 130022, China*

Cite this article: *Nano Research*, **2026**, *19*, 94908396. https://doi.org/10.26599/NR.2026.94908396

ABSTRACT: Despite the great interest in the safe and compact storage of hydrogen in the form of metal-hydrides, obtaining alloys capable of reversibly and rapidly storing large amounts of hydrogen at ambient conditions represents a challenge. High-entropy alloys (HEAs) have great potential for hydrogen storage (HS) applications because of their broad compositional design space. In this study, we designed and synthesized $V_{35}Ti_{35}Cr_{10}Fe_{20-x}Mn_x$ (x = 6, 8, 10, 12, and 14) alloys based on high entropy engineering for room temperature HS. With an increase in the Mn/Fe ratio, the abundance of the body-centered cubic (BCC) phase gradually increased until the formation of a single-phase BCC-structured solid-solution alloy. The $V_{35}Ti_{35}Cr_{10}Fe_6Mn_{14}$ alloy reached 3.79 wt.% of hydrogen absorption at 298 K, which is the highest capacity reported for HEAs. All alloys were fully activated in one hydrogen ab/desorption cycle and saturated with hydrogenation within 100 s. Quasi-*in situ* X-ray diffraction characterization of the hydrogenation of HEAs revealed a phase transition from BCC to face-centered cubic (FCC) with an intermediate pseudo-BCC structure. The cycling characteristics of the alloys evidenced that their stability gradually increased with decreasing Mn content. The microstructural analysis revealed that the capacity decay of HEAs during cycling is mainly caused by lattice deformation from repeated expansion and contraction. In addition, the HS properties of HEAs were investigated by a combination of first-principles simulation and experiments. Moreover, the thermal conductivity of the alloys was investigated. This work provides new perspectives for the design of HS alloys that can rapidly absorb large amounts of hydrogen under ambient conditions.

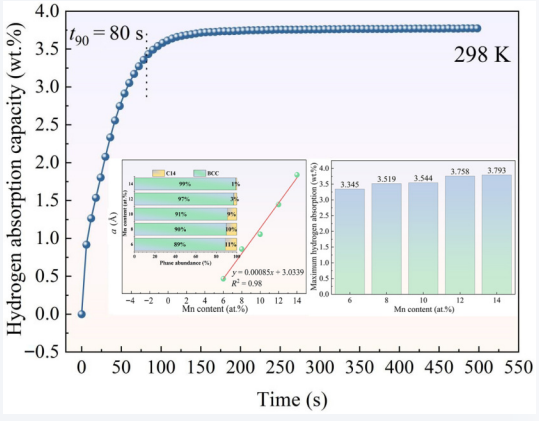

KEYWORDS: high entropy alloys, solid-state hydrogen storage, kinetic properties, thermal conductivity, first-principles simulation

1 Introduction

With continuous societal development, the demand for energy is increasing. Traditional energy sources are mainly derived from fossil fuels that negatively impact the environment during extraction and combustion, thereby representing one of the most important contributors to the greenhouse effect [1]. Hydrogen, as a clean and efficient energy carrier, has the advantages of high energy density (120–142 MJ/kg) and abundance combined to a pollution-free combustion process. Therefore, hydrogen-related technologies are constantly being sought to meet various challenges, including efficient hydrogen production [2, 3] and storage technologies [4]. Hydrogen storage methods are mainly divided into three types: high-pressure gaseous (usually 350 or 700 bar), low-temperature

Received: October 30, 2025; **Revised:** December 17, 2025
Accepted: December 31, 2025

✉Address correspondence to Yuan Deng, bfxtdy@163.com; Bingbing Chen, chenbb@njtech.edu.cn; Yongzhi Li, liyzh1983@imust.edu.cn

liquid (below −252 °C), and solid-state hydrogen storage [5], the latter having the advantages of high hydrogen storage density, easy transportation, and safety. Solid-state hydrogen storage is mainly based on metal hydrides such as Mg- [6], TiFe- [7], V- [8], and Zr-based hydrides [9]. Each has its own advantages, but all of them have some problems that currently represent a bottleneck for the development of the metal-hydride solid-state hydrogen storage industry [10–13].

Yeh et al. [14] introduced the concept of high entropy alloys (HEAs) based on multi-major element alloys. HEAs are defined as alloys with five or more elements, with the concentration of each major element ranging from 5 at.% to 35 at.%. The synergistic effect between the elements provides HEAs with unique properties including high strength/hardness, excellent wear resistance, good structural stability, and good corrosion and oxidation resistance. These characteristics have continuously attracted the attention of researchers as HEAs play an important role in several material fields [14–19]. More interestingly, the high mixing entropy in multi-primary element alloys can significantly reduce the free energy of the entire alloy system, which facilitates the formation of stable solid solution phases such as body-centered cubic (BCC), face-centered cubic (FCC), and hexagonal close-packed (HCP) lattices. HEAs have a wide scope for compositional design, and their capacity to sustain high lattice distortions results in the formation of numerous sites favorable for hydrogen absorption, which could potentially eliminate the bottleneck hindering the use of metal hydrides for solid-state hydrogen storage.

In 2010, Kao et al. [20] first investigated HEAs as hydrogen storage materials and reported a hydrogen storage capacity of 1.82 wt.%. Since then, researchers have explored different HEAs for hydrogen storage [21–23]. Zlotea et al. [24] investigated the effect of composition on the hydrogen storage properties of a range of refractory HEAs: $Ti_{0.30}V_{0.25}Zr_{0.10}Nb_{0.25}M_{0.10}$ (M = Mg, Al, Cr, Mn, Fe, Co, Ni, Cu, Zn, Mo, and Ta), and the effect of the addition of 10 at.% of M on the hydrogen storage properties of Ti-V-Zr-Nb HEAs was comprehensively evaluated. These studies demonstrate that HEAs have great application potential in the field of hydrogen storage. However, there are some drawbacks such as activation difficulties, low hydrogen storage capacity, relatively high temperatures required for hydrogen storage, and poor cycling stability [25–28]. Therefore, further development of hydrogen-storage HEAs with improved performance is required.

Building on our previous discovery of the promising hydrogen storage performance (high capacity and good kinetics) in a V-Ti-Cr-Fe-Mn alloy [29], the present work investigates the strategic substitution of Fe with Mn. This substitution is inspired by the larger atomic radius of Mn, which expands the BCC lattice parameter, a key factor for enhancing hydrogen storage capacity. Furthermore, Mn offers economic and weight advantages. Guided by the HEA design, a series of $V_{35}Ti_{35}Cr_{10}Fe_{20-x}Mn_x$ (x = 6, 8, 10, 12, and 14) alloys were prepared. Their microstructure, hydrogen storage properties, cycling stability, and thermal conductivity were systematically examined through integrated theoretical and experimental studies. This research provides new insights for developing advanced alloys capable of efficient hydrogen absorption at room temperature (RT).

2 Materials and methods

2.1 Alloy designs

The phase structure of HEAs has a very important impact on their properties; thus, the phase prediction helps in designing HEAs for specific requirements, and some empirical parameters have been proposed by researchers based on the Hume–Rothery rule. For example, the atomic size difference (δ) affects the crystal structure, hydrogen absorption activity, crystal defects, diffusion properties, and phase stability of HEAs, which in turn affect their hydrogen storage properties. Alloys with $\delta \leq 6.5\%$ are more likely to form solid solution phase [30]. The parameter δ is expressed as follows

$$\delta = 100\sqrt{\sum_{i=1}^{n} c_i \left(1 - \frac{r_i}{\bar{r}}\right)^2} \quad (1)$$

where n is the number of group points, c_i is the percentage of the i^{th} group atoms, r_i is the atomic radius of the i^{th} element, and $\bar{r}$ is the average atomic radius ($\bar{r} = \sum_{i=1}^{n} c_i r_i$).

Variations in the valence electron concentration (VEC) affect the electronic structure of hydrogen storage high-entropy alloys, which in turn affects their physical and chemical properties. VEC is a physical parameter that controls the stability of FCC or BCC solid solution phases and is expressed as

$$\mathrm{VEC} = \sum_{i=1}^{n} c_i \mathrm{VEC}_i \quad (2)$$

where VEC_i is the valence electron concentration of the i^{th} element and c_i is the atomic percentage of the i^{th} element. HEAs are more likely to form BCC phases when VEC < 6.87 and FCC phases when VEC > 8 [31].

The thermodynamic parameter Ω, which represents the balance between entropy and enthalpy of mixing, has been used to estimate the solid solution formation capacity in multicomponent alloy systems. $\Omega \geq 1.1$ with $\delta \leq 6.6\%$ is required for the formation of stable solid solution phases [32]. The parameter Ω is defined as follows

$$\Omega = \frac{T_{\mathrm{m}} \Delta S_{\mathrm{mix}}}{|\Delta H_{\mathrm{mix}}|} \quad (3)$$

where $T_{\mathrm{m}} = \sum_{i=1}^{n} c_i (T)_{\mathrm{m}i}$, and $(T)_{\mathrm{m}i}$ is the melting point of the i^{th} component, while ΔH_{mix} and ΔS_{mix} are the enthalpy and entropy of mixing, respectively. Zhang et al. [24] demonstrated that the solid solution phase is formed more easily at −15 kJ/mol < ΔH_{mix} < 5 kJ/mol and 12 J/(K·mol) < ΔS_{mix} < 17.5 J/(K·mol). ΔH_{mix} and ΔS_{mix} are defined as follows

$$\Delta H_{\mathrm{mix}} = \sum_{i=1, i \neq j}^{n} \Omega_{ij} c_i c_j \quad (4)$$

$$\Delta S_{\mathrm{mix}} = -R \sum_{i=1}^{n} c_i \ln c_i \quad (5)$$

where c_i and c_j denote the atomic percentage of the i^{th} and j^{th} components, respectively, while $\Omega_{ij} = 4\Delta H_{\mathrm{AB}}^{\mathrm{mix}}$, and $\Delta H_{\mathrm{AB}}^{\mathrm{mix}}$ is the enthalpy of mixing of the binary liquid alloy. R is the gas constant (R = 8.314 J/(K·mol)).

Table 1 lists the data used to calculate the empirical parameters for the HEAs, and the corresponding calculated values are summarized in Table 2. According to the data in Table 2, the entropy–enthalpy ratio parameter Ω for this series of alloys is greater than 1.1, and the atomic size difference δ is less than 6.5%, which together satisfy the thermodynamic and geometric conditions for forming a stable solid solution. Furthermore, the VEC of all alloys is significantly lower than 6.87. Based on the classical empirical criteria mentioned above, this strongly indicates a tendency to form a BCC structure. Therefore, the theoretical

Table 1 Data used to calculate ΔH_{mix}, Ω, δ, and VEC for the V-Ti-Cr-Fe-M system [33, 34]

Element i	r (pm)	ΔH^{ij}_{mix}(kJ/mol)					T_m (K)	VEC$_i$
		V	Ti	Cr	Fe	Mn		
V	131.60	—	−2	−2	−7	−1	2183	5
Ti	146.15	−2	—	−7	−17	−8	1941	4
Cr	124.91	−2	−7	—	−1	2	2180	6
Fe	124.12	−7	−17	−1	—	0	1811	8
Mn	135.00	−1	−8	2	0	—	1519	7

Table 2 Calculated parameters for the selected compositions

Alloys	ΔS_{mix} (J/(K·mol))	ΔH_{mix} (kJ/mol)	Ω	δ (%)	VEC
$V_{35}Ti_{35}Cr_{10}Fe_{14}Mn_6$	11.72	−7.708	3.03	6.376	5.29
$V_{35}Ti_{35}Cr_{10}Fe_{12}Mn_8$	11.82	−7.264	3.25	6.258	5.27
$V_{35}Ti_{35}Cr_{10}Fe_{10}Mn_{10}$	11.85	−6.820	3.46	6.134	5.25
$V_{35}Ti_{35}Cr_{10}Fe_8Mn_{12}$	11.82	−6.376	3.69	6.004	5.23
$V_{35}Ti_{35}Cr_{10}Fe_6Mn_{14}$	11.72	−5.932	3.94	5.868	5.21

parameters collectively demonstrate that the designed compositions will form a BCC solid solution, which ensures efficient hydrogen absorption.

2.2 Alloy preparation

$V_{35}Ti_{35}Cr_{10}Fe_{20-x}Mn_x$ (x = 6, 8, 10, 12, and 14) HEAs were prepared from Ti (99.95%), V (99.95%), Cr (99.99%), Fe (99.95%), and Mn (99.90%) in an arc-melting furnace with a water-cooled copper crucible under an argon atmosphere. All metals were purchased from Beijing Ryubon New Material Technology Co., Ltd. Because the saturated vapor pressure of Mn is high, it tends to volatilize during melting. Therefore, an additional 5 wt.% of Mn was added to achieve the desired stoichiometry during melting. The mixture was turned and melted five more times during melting to ensure the uniformity of the alloy composition. Finally, the button ingots (~ 50 g) were mechanically crushed in air and then sieved through a 200 mesh sieve.

2.3 Microstructural characterization

The phase composition and crystal structure of the alloys were determined by X-ray diffraction (XRD; BRUKER, D8 ADVANCE; λ = 1.5418 Å, 45 kV, 40 mA, scanning range: 2θ = 20°–120°, scanning speed: 2.5 °/min, and step size: 0.01°) and by field emission scanning electron microscopy (CIQTEK Co., Ltd., FESEM5000X, 15 kV) combined with energy dispersive spectroscopy. The alloy microstructure was imaged using field emission transmission electron microscopy (FE-TEM; JEM-2100F, 200 kV).

2.4 Hydrogen storage properties

For each experiment, approximately 1.2 g of the sample was placed in the sample tube, and a Sievert-type apparatus (high pressure pressure-composition-temperature (PCT) adsorption analyzer, H-Sorb 2600PCT, CIQTEK Co., Ltd.) was used to activate the sample and test its hydrogen storage performance. First, the tubes were evacuated directly at room temperature (298 K) for 30 min using a thermostatic water bath (Runner HH-8) to ensure a stable environment. Then, the hydrogen pressure in the system was raised to 5 MPa and the amount of hydrogen absorbed was monitored until it reached a stable value, after which the samples were completely dehydrogenated by evacuation for 1 h at 673 K. This process was repeated until the alloys were completely activated. The hydrogen absorption kinetics of the alloys were then tested at room temperature and hydrogen pressure of 5 MPa. Following the saturation of hydrogen absorption, the hydrogen release kinetics were tested at temperatures of 298, 315, 335, and 355 K. Finally, PCT curves were measured at 298, 315, 335, and 355 K to determine the thermodynamic properties of the alloys.

The cycling characteristics of the alloys were investigated at 298 K under hydrogen pressure of 5 MPa for 1 h. Complete dehydrogenation was performed at 673 K for 1 h. The above steps were repeated 50 times, the hydrogen absorption data were continually recorded, and the capacity retention rate was calculated for each alloy.

2.5 Thermal conductivity measurement

The thermal diffusivity of the alloys was tested using the laser flash method. Before the test, the alloy powder crushed to 200 mesh was pressed into a disc-like sample with a diameter of 12.7 mm and a thickness of about 2 mm under the forming pressure of 750, 1125, and 1500 MPa. After spraying graphite on both sides of the formed alloy disc, one surface of the test sample was irradiated with a pulse laser (pulse width of 0.6 milliseconds) in a laser thermal conductivity meter (NETZSCH, LAF467). The surface began to heat up, and a detector was used to monitor the rise in temperature on the back side over time. After obtaining the thickness of the disc-shaped sample, the thermal diffusivity of the sample could be calculated by measuring the temperature rise on the back of the sample over time. Following the same test procedure, the specific heat capacity of the sample to be tested could be calculated by referencing the sample to a graphite standard sample.

2.6 Computational methods

The Vienna *ab initio* package (VASP) was employed to perform all the density functional theory (DFT) calculations within the generalized gradient approximation (GGA) using the Perdew, Burke, and Enzerhof (PBE) formulation [35–37]. The projected augmented wave (PAW) potentials were applied to describe the ionic cores and take valence electrons into account using a plane wave basis set with a kinetic energy cutoff of 500 eV [38, 39]. Special quasi-random structure (SQS) models were used for creating the structure model of the solid solution alloys. Partial occupancies of the Kohn–Sham orbitals were allowed using the Gaussian smearing method with a width of 0.05 eV. The electronic energy was considered self-consistent when the energy change was smaller than 10^{-5} eV. A geometry optimization was considered convergent when the force change was smaller than 0.05 eV/Å. Grimme's DFT-D3 methodology was used to describe the dispersion interactions [40]. The vacuum spacing perpendicular to the plane of the structure was 20 Å. The dissociation energy was also calculated. The Brillouin zone integral utilized the surface structures of 2 × 2 × 1 monkhorst pack K-point sampling. Finally, the adsorption energies (E_{ads}) were calculated as $E_{ads}= E_{ad/sub} - E_{ad} - E_{sub}$, where $E_{ad/sub}$, E_{ad}, and E_{sub} are the total energies of the optimized adsorbate/substrate system, the adsorbate in the structure, and the clean substrate, respectively. The free energy was calculated using the equation

$$G = E_{ads} + \mathrm{ZPE} - TS \quad (6)$$

where G, E_{ads}, ZPE, and TS are the free energy, total energy from DFT calculations, zero point energy, and entropic contributions, respectively. Finally, the formation energy (E_f) of a compound was defined, as given in Eq. 7

$$E_f = E_{total} - N_V\mu_V - N_{Fe}\mu_{Fe} - N_{Cr}\mu_{Cr} - N_{Mn}\mu_{Mn} - N_{Ti}\mu_{Ti} \quad (7)$$

where E_{total} is the total DFT energy of a given structure, and μ{V, Fe, Cr, Mn, Ti} are the chemical potentials of the constituent atomic species, and N{V, Fe, Cr, Mn, Ti} are the number of the constituent atomic species.

3 Results and discussion

3.1 Microstructure

Figure 1(a) shows the XRD profiles of the as-cast $V_{35}Ti_{35}Cr_{10}Fe_{20-x}Mn_x$ (x = 6, 8, 10, 12, and 14) HEAs, thereafter the samples are labeled Mn6, Mn8, Mn10, Mn12, and Mn14, respectively. The analysis of the XRD profiles shows that the main phase of all alloys is the BCC solid solution phase, which is consistent with the phase prediction in Section 2.1, indicating that the combined consideration of Ω, δ, and VEC can effectively predict the phase of the alloys. The amount of the second phase, the C14 Laves phase, decreased as the Mn content of the alloy increased. Figure 1(b) shows the magnification of the main peak of the BCC phase (011), where a gradual shift of the peak to the left with an increase in the Mn content of the alloy is evidenced, indicating that the lattice constant gradually increased. To obtain more detailed microstructural information, the XRD patterns of the five alloys were refined, as shown in Figs. 1(c)–1(g), and the results of the Rietveld refinement are listed in Table 3. A slight linear increase in the lattice constant of the main phase of BCC is observed with the increase of Mn/Fe ratio, as displayed by the relationship between the lattice constant of the alloys and the Mn content in Fig. 1(h), which is in accordance with Vegard's law [41]. The phase abundance of the BCC structure increases with the increase of the Mn content. For Mn10, the grain size was estimated to be ~ 20 nm using the Scherrer equation [42]. Figure 1(i) shows the backscattered electron (BSE) images of the as-cast $V_{35}Ti_{35}Cr_{10}Fe_{20-x}Mn_x$ (x = 6, 8, 10, 12, and 14) HEAs, where two regions with different linings represent two different phases. An increase in the Mn content results in a gradual decrease of the second phase, which is consistent with the XRD results and related to the fact that Fe is mainly distributed in the C14 Laves phase and plays a dominant role in its lattice changes [43].

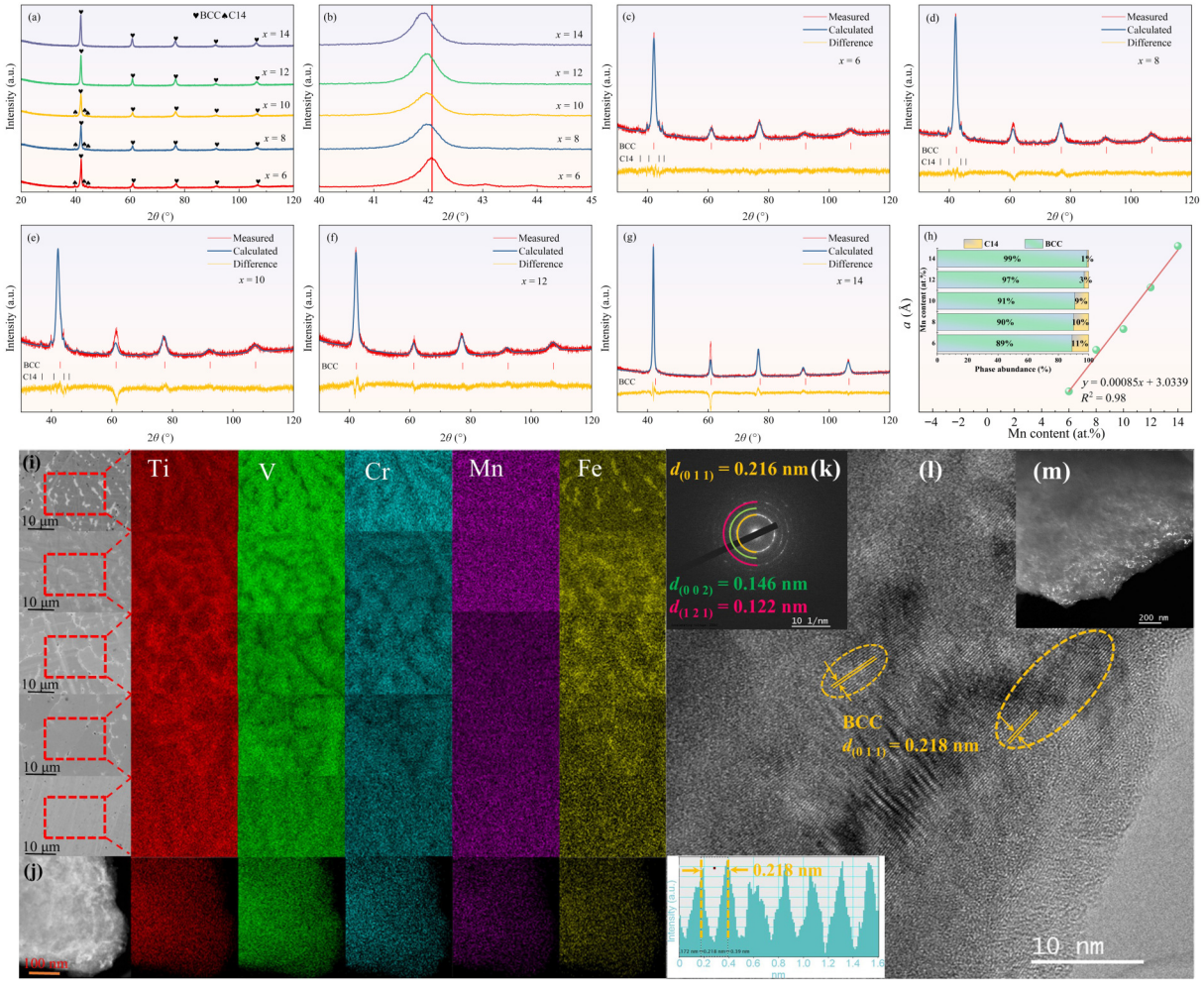

Figure 1 XRD patterns of the $V_{35}Ti_{35}Cr_{10}Fe_{20-x}Mn_x$ (x = 6, 8, 10, 12, and 14) alloys: (a) 2θ = 20°–120° and (b) 2θ = 40°–45°. (c)–(g) Rietveld profile fitting of the XRD patterns. (h) Relationship between the BCC lattice constant and Mn content. (i) BSE micrographs and EDS elemental mappings. (j) EDS mapping analysis under TEM, (k) SAED diffraction patterns, (l) HRTEM image, and (m) TEM dark-field image of the of the Mn10 alloy.

Table 3 Rietveld refinement characteristics of the $V_{35}Ti_{35}Cr_{10}Fe_{20-x}Mn_x$ alloys XRD patterns

Sample	Phase	Space group	Lattice constants		Abundance (%)	R_{wp} (%)	S
			a (Å)	c (Å)			
x = 6	BCC	$Im\bar{3}m$(229)	3.039(1)	—	89	4.07	1.21
	C14	$P6_3/mm$ (194)	4.831(3)	8.074	11		
x = 8	BCC	$Im\bar{3}m$ (229)	3.041(1)	—	90	4.21	1.31
	C14	$P6_3/mmc$ (194)	4.919(2)	8.023	10		
x = 10	BCC	$Im\bar{3}m$ (229)	3.042(4)	—	91	5.32	1.52
	C14	$P6_3/mmc$ (194)	4.904(3)	8.005	9		
x = 12	BCC	$Im\bar{3}m$ (229)	3.044(1)	—	97	5.03	1.32
	C14	$P6_3/mmc$ (194)	4.749(2)	7.991	3		
x = 14	BCC	$Im\bar{3}m$ (229)	3.046(2)	—	99	6.44	1.72
	C14	$P6_3/mmc$ (194)	4.843(4)	8.061	1		

A TEM analysis of the representative alloy $V_{35}Ti_{35}Cr_{10}Fe_{10}Mn_{10}$ was performed to further investigate the microstructure of the alloy, as shown in Figs. 1(k)–1(m). Figure 1(j) shows the energy dispersive X-ray spectroscopy (EDS) analysis under transmission electron microscopy, which shows that the composition of the alloy is homogeneous on the nanoscale. The dark-field image in Fig. 1(m) shows a distinct nanocrystalline structure with estimated grain sizes in the range of 10–30 nm, which is in agreement with that estimated using the Scherrer equation. Figure 1(k) presents the selected area electron diffraction (SAED) patterns, which exhibits ring features characteristic of polycrystalline or nanocrystalline materials. The analysis of these patterns, combined with the high-resolution TEM (HRTEM) image in Fig. 1(l), confirms the presence of a BCC phase in the alloy. The measured interplanar spacing of 0.217 nm in Fig. 1(l) corresponds to the (011) plane of the BCC structure.

3.2 Hydrogen absorption and desorption kinetics

3.2.1 *Hydrogen absorption kinetics*

The activation process and hydrogen uptake kinetics of the five HEAs are shown in Figs. 2(a)–2(e), respectively. The $V_{35}Ti_{35}Cr_{10}Fe_{20-x}Mn_x$ (x = 6, 8, 10, 12, and 14) HEAs were activated at 298 K under a hydrogen pressure of 5 MPa, and then passed directly into the sample chamber. All alloys were fully activated during the second hydrogen uptake, and they showed excellent activation performance, mainly because of the high-density crystal interfaces in their nanostructure, which provides more channels for hydrogen diffusion [44]. With the gradual substitution of Mn atoms for Fe, the BCC phase content, lattice constant, and maximum hydrogen absorption of the alloy gradually increased, as shown in Fig. 2(f), HEA-14 exhibits a maximum hydrogen absorption capacity of 3.793 wt.%, which is higher than the hydrogen absorption of any of the hydrogen-storing HEAs reported so far. This suggests that it possesses both a high abundance of the hydrogen absorbing main phase and a large lattice constant that provide larger interstitial sites, both of which favor hydrogen absorption [45]. In addition, $V_{35}Ti_{35}Cr_{10}Fe_{20-x}Mn_x$ (x = 6, 8, 10, 12, and 14) alloys reached 90% of the saturated hydrogen uptake at approximately 80 s ($t_{0.9}$). Crystal defects, with grain boundaries as a typical example, provide favorable channels for hydrogen diffusion and enhance hydrogenation kinetics [46–48]. The nanocrystals had a mean diameter ranging from 10 to 30 nm, yielding a grain boundary area density of approximately 1×10^9 m^2/m^3, substantially higher than the typical grain boundary density of 10^4–10^5 m^2/m^3 found in microcrystalline counterparts [49, 50]. The abundant grain boundaries and interfaces in such nanocrystalline alloys can serve as efficient transport pathways for hydrogen atoms from the surface to the bulk interior, thereby enhancing the hydrogen absorption kinetics of the HEAs. The XRD patterns of the five alloys following hydrogen saturation (Fig. 3(a)) show the presence of three phases (BCC, FCC, and C14). This is due to the fact that the C14 Laves phase does not undergo a phase transition after hydrogen absorption [51, 52], whereas the hydrogen atoms occupy the tetrahedral and octahedral interstices as they enter the BCC structure, which is then transformed into the FCC structure [53, 54]. The presence of the BCC phase is primarily attributed to the partial decomposition of the formed dihydride under ambient conditions. The underlying reason is thermodynamic in nature: The dihydride in this alloy system is not stable at standard atmospheric pressure (~ 0.1 MPa) and room temperature. Therefore, during the necessary yet unavoidable transfer of the fully hydrogenated sample from the sealed reaction chamber to the XRD instrument, the sample is briefly exposed to air (ambient pressure). Even within this short period, driven by the pressure difference, the dihydride phase undergoes a partial reversible decomposition reaction.

VEC and δ are not only important for predicting the phase of HEAs, but also play a key role in the evaluation of hydrogen storage performance. Nygård et al. [55] demonstrated that the hydrogen storage capacity decreases with the increase of VEC for VEC > 5.17, as displayed in the diagram of the maximum saturated hydrogen adsorption (abs.) vs. δ and VEC for the $V_{35}T_{i35}Cr_{10}Fe_{20-x}Mn_x$ (x = 6, 8, 10, 12, and 14) alloys (Fig. 3(b)). A smaller δ promotes the formation of a more homogeneous solid solution with reduced lattice distortion. This uniformity increases the availability and energetical consistency of interstitial sites for hydrogen occupation, thereby enhancing the hydrogen storage capacity. In summary, VEC and δ have important effects on the hydrogen capacity of the alloys, with lower VEC and smaller δ both favoring large hydrogen absorption capacity.

3.2.2 *Hydrogen desorption kinetics*

The hydrogen release kinetics of the$V_{35}Ti_{35}Cr_{10}Fe_{20-x}Mn_x$ (x = 6, 8, 10, 12, and 14) HEAs were tested at 298, 315, 335, and 355 K after saturated hydrogen absorption at 298 K and are shown

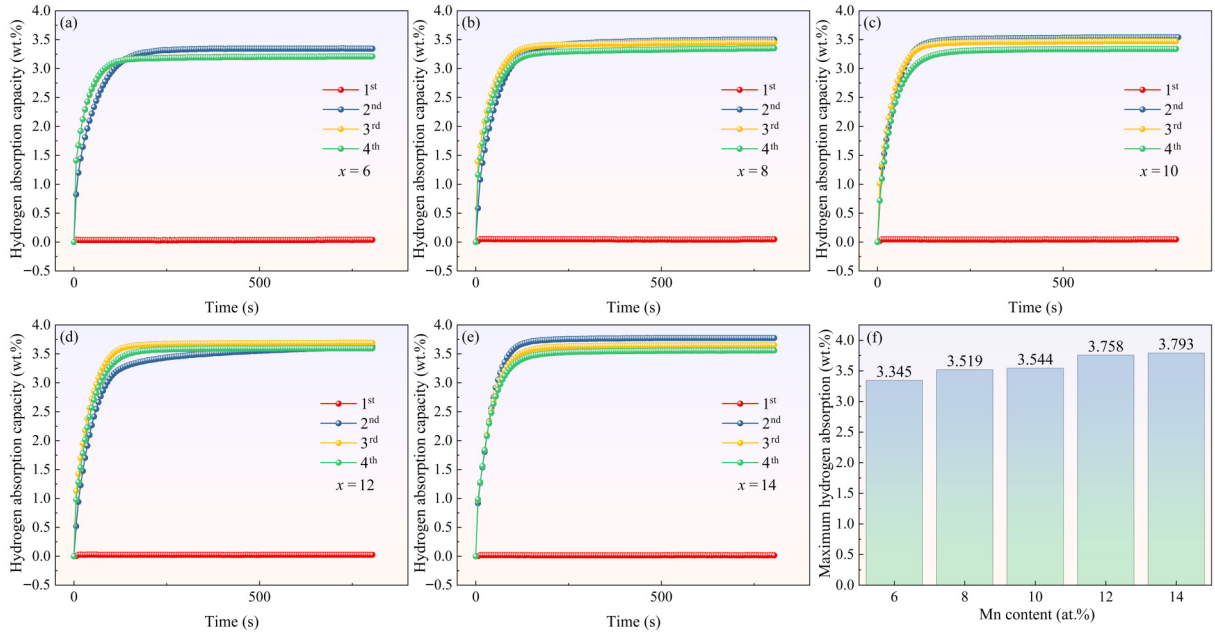

Figure 2 (a)–(e) Hydrogenation kinetics curves of $V_{35}Ti_{35}Cr_{10}Fe_{20-x}Mn_x$ (x = 6, 8, 10, 12, and 14) alloys. (f) Relationship between maximum hydrogen absorption capacity and Mn content.

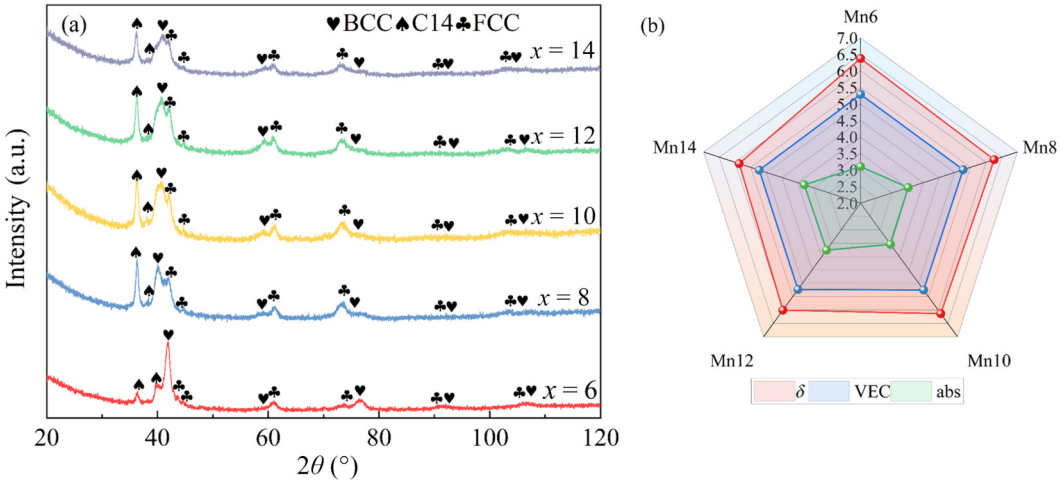

Figure 3 (a) XRD patterns of hydrogenated $V_{35}Ti_{35}Cr_{10}Fe_{20-x}Mn_x$ (x = 6, 8, 10, 12, and 14) HEAs. (b) Diagram of the relationship between δ, VEC, and maximum hydrogen absorption.

in Figs. 4(a)–4(e), evidencing that the hydrogen release properties of the alloys are completely different at different temperatures. At 298 K, the hydrogen release capacity of the five alloys decreased in the order of Mn6 > Mn8 > Mn10 > Mn12 > Mn14, and the order of the hydrogen release kinetics was Mn6 > Mn14 > Mn10 > Mn12 > Mn8. At 315 K, the order of the hydrogen release capacity was Mn12 > Mn10 > Mn6 > Mn14 > Mn8, and the order of the hydrogen release kinetics was Mn6 > Mn10 > Mn8 > Mn12 > Mn14. At 355 K, the order of hydrogen release capacity was the same, as shown in Fig. 4(f), with a maximum for Mn12 (1.949 wt.%), and the order of hydrogen release kinetics was Mn6 > Mn10 > Mn8 > Mn14 > Mn12. Interestingly, Mn6 exhibits excellent hydrogen release kinetics at all four temperatures, which is attributed to the fact that it possesses a smaller lattice constant. The different hydrogen release properties are closely related to the thermodynamics and microstructure, which is discussed in detail below [56, 57].

3.3 Thermodynamic characteristic

The hydrogen storage properties of the five alloys were investigated using PCT curves at temperatures of 298, 315, 335, and 355 K, as shown in Figs. 5(a)–5(e). Three main regions in the process of hydrogen uptake are observed: The first is the sharp increase in pressure at low hydrogen content, the second represents a plateau region, and the third one is another sharp increase of the pressure with the increase in hydrogen content. For each alloy, the pressure in the plateau region gradually increases with increasing temperature, whereas the plateau region shortens, which leads to a decrease in the hydrogen absorption capacity of the alloy with increasing temperature [58, 59]. Moreover, the hysteresis decreases with increasing temperature, which may result from thermally activated stress relaxation processes. The hysteresis is a measure of the energy loss during the hydrogen uptake/desorption cycle, which stems from the transformation of the metal hydride, resulting in the

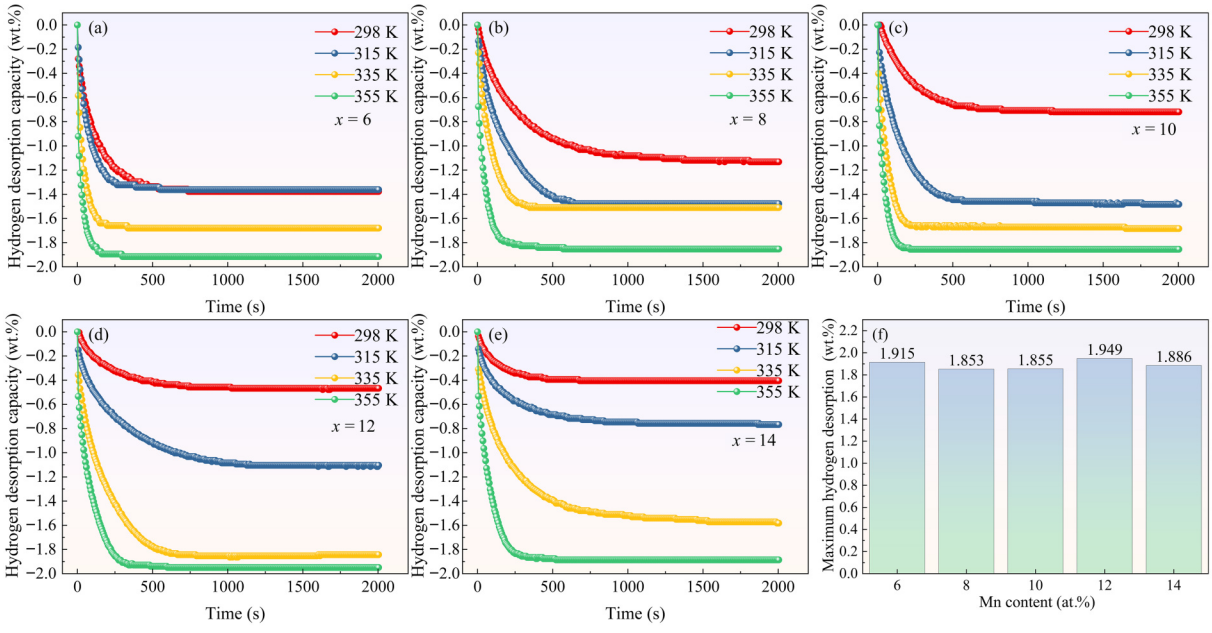

Figure 4 (a)–(e) Dehydrogenation kinetics curves of $V_{35}Ti_{35}Cr_{10}Fe_{20-x}Mn_x$ (x = 6, 8, 10, 12, and 14) alloys. (f) Relationship between maximum hydrogen desorption capacity and Mn content.

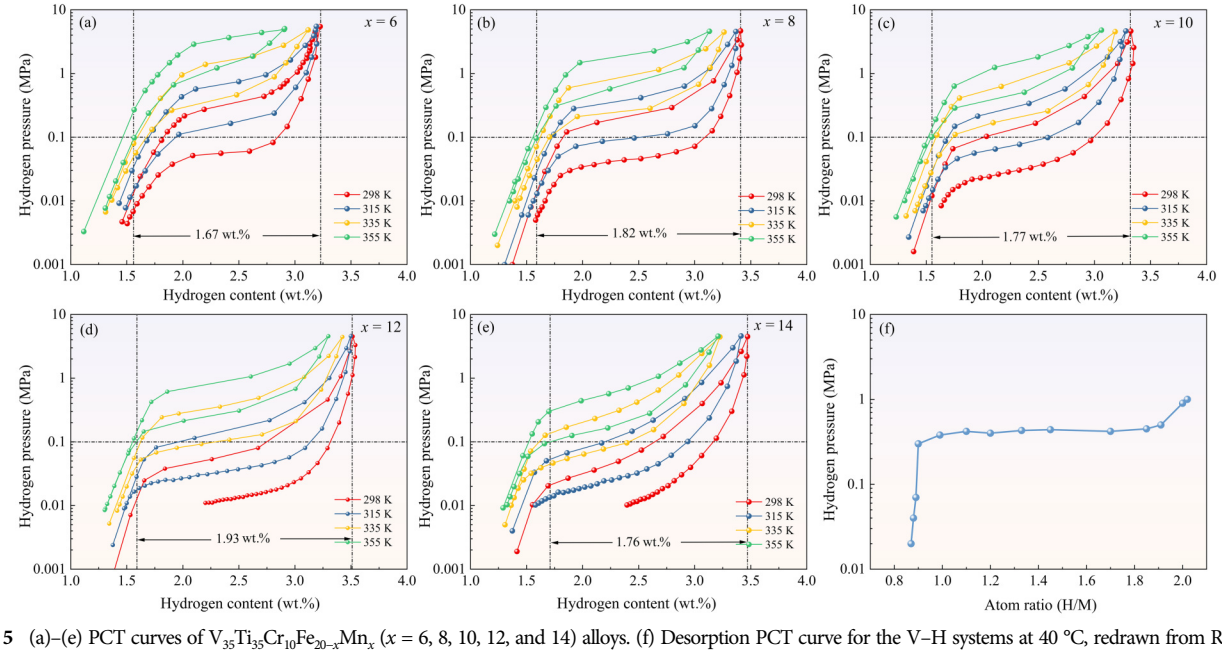

Figure 5 (a)–(e) PCT curves of $V_{35}Ti_{35}Cr_{10}Fe_{20-x}Mn_x$ (x = 6, 8, 10, 12, and 14) alloys. (f) Desorption PCT curve for the V–H systems at 40 °C, redrawn from Ref. [62].

strain and generation of internal defects such as dislocations, stacking, and laminar faults. An increase in temperature therefore improves the effective hydrogen release [57]. After achieving hydrogen saturation at 298 K, the $V_{35}Ti_{35}Cr_{10}Fe_{20-x}Mn_x$ (x = 6, 8, 10, 12, and 14) series of high-entropy alloys were heated to 355 K, and hydrogen desorption tests were conducted with a cutoff pressure of 0.1 MPa. The measured effective reversible hydrogen storage capacities were 1.67 wt.%, 1.82 wt.%, 1.77 wt.%, 1.93 wt.%, and 1.76 wt.%, respectively, which aligns with the previously mentioned hydrogen release kinetics trends. To further investigate the origin of the gradual decrease in hydrogen release at room temperature for the $V_{35}Ti_{35}Cr_{10}Fe_{20-x}Mn_x$ (x = 6, 8, 10, 12, and 14) HEAs, we compared their PCT curves at 298 K. The results showed that the plateau pressures gradually decreased with increasing Mn content. Thus, to achieve the same hydrogen release as that of Mn6, the other four alloys required lower pressures. It is also observed that, at the same temperature, the slope of the plateau gradually increased as the proportion of Mn atoms increased. As shown in Fig. 5(f), the hydrogen uptake PCT curve of pure vanadium exhibits a distinct plateau region compared to that of the alloys in this study. Therefore, the gradual increase in the plateau slope is due to the gradual increase in the local chemical potential difference. For the five alloys at all temperatures, no complete hydrogen desorption was observed, which is not only related to the thermodynamic properties but also to the presence of strong hydrogen-absorbing elements (Ti and V) that have a stronger binding energy with hydrogen, thereby requiring more energy to achieve complete desorption [60, 61].

As can be seen from Figs. 4 and 5, the hydrogen desorption capacity of BCC high-entropy alloys is lower than their hydrogen absorption capacity. The core reason lies in the thermodynamic irreversibility. The PCT curves exhibit two plateau regions: The first plateau (not visible in Fig. 5 due to its extremely low plateau pressure) corresponds to the phase transformation from the hydrogen-containing solid solution phase to the monohydride phase, which is thermodynamically highly stable and difficult to desorb at moderate temperatures. The second plateau (as shown in Fig. 5) corresponds to the transformation of the monohydride phase into the dihydride phase upon hydrogen absorption. The dihydride phase is relatively unstable and can release hydrogen even at room temperature. Moreover, as can be observed in Fig. 5, there is significant pressure hysteresis in the dissociation of the dihydride. Under room temperature and ambient pressure conditions, once the hydrogen-saturated dihydride desorbs back to the monohydride phase, the latter cannot spontaneously decompose further because its equilibrium dissociation pressure is far below the system pressure. This results in an "irreversible capacity", where this portion of hydrogen remains "locked" within the lattice, leading to a significantly lower desorption capacity compared to the total absorption capacity.

To further analyze the effect of Mn content on the thermodynamic properties of the alloys, we calculated the entropy (ΔS) and enthalpy (ΔH) changes during the hydrogen absorption and discharge process using the Van't Hoff equation and the following expressions

$$\ln\frac{P_{eq}}{P_0} = \frac{\Delta H}{RT} - \frac{\Delta S}{R} \tag{8}$$

where P_{eq} denotes the plateau pressure, T is the temperature, and P_0 is the standard atmospheric pressure. The Van't Hoff plots (Figs. 6(a)–6(e)) clearly evidence that the absolute value of ΔH gradually increases with increasing Mn/Fe ratio. This is due to the fact that the BCC lattice constant accordingly gradually increases, so the hydrogen atoms are more stable after the formation of the hydrides [8], which explains why Mn14 has the lowest hydrogen release at room temperature.

To gain a deeper understanding of the phase transformation of the alloy during hydrogen uptake, we performed an XRD analysis of Mn10 at different hydrogen uptake stages. The XRD patterns are shown in Fig. 6(f) for the pristine sample and following hydrogen uptake of 25%, 50%, 75%, and 100%. During hydrogenation, hydrogen atoms gradually diffuse into the alloy crystal structure and adsorb onto lattice vacancies or other suitable locations. For hydrogen absorption of 25% and 50%, the alloy maintained the BCC structure, but the position of the BCC (011) plane peak was significantly shifted, indicating that the crystal lattice was deformed. The single-phase absorption intervals ranged from H/M atom ratios of 0.5 to 1.0 at 298 K, where the peaks corresponded to the BCC (011) plane. As the alloy continued to absorb hydrogen, part of the pseudo-BCC phase gradually transformed into the FCC phase, and two structures (pseudo-BCC + FCC) coexisted when 75% of the hydrogen absorption was reached, whereas the hydride phase is FCC once the alloy was fully hydrogenated. The small amount of pseudo-BCC phase that was still present after complete hydrogenation may be due to the partial decomposition of the fully hydrogenated samples in air during their transfer from the sample chamber to that used for XRD measurements [29].

3.4 Theoretical analysis

Figure 7(a) shows one example of modeled structure of HEA-10 alloy before and after the hydrogen absorption, which was modeled using the SQS and visualized using VESTA software. Formation energy is an important parameter to indicate the stability of a compound. A negative E_f indicates the stability of substitution structure. Figure 7(b) shows the formation energies for BCC-structured $V_{35}Ti_{35}Cr_{10}Fe_{20-x}Mn_x$ (x = 0, 6, 8, 10, 12, and 14) alloys. All substituted unit cells exhibit the negative E_f rang of −4.1258 to −2.1232 eV, indicating that all substituted structures exhibit stable BCC structure. The structural stability obtained from formation enthalpy calculations agree well with the results of the alloy designs in Section 2.1. According to the rule, alloy is more likely to form a solution solid with BCC structure rather than a compound when the atomic size difference is less than 6.5% and VEC is less than 6.87. The data in Table 2 show that the atomic size difference and

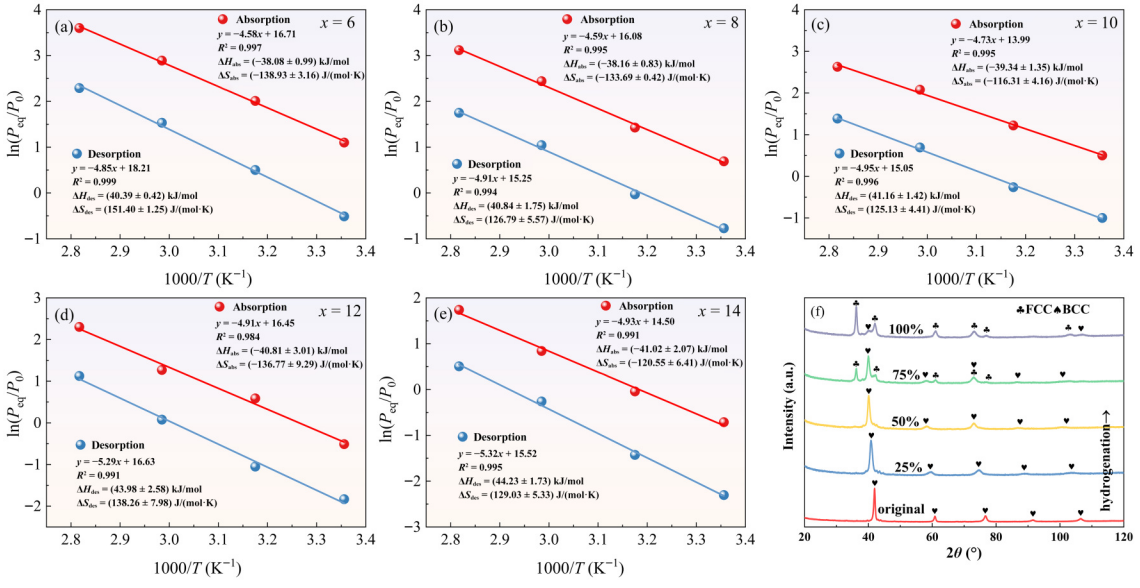

Figure 6 (a)–(e) The Van't Hoff plots of the$V_{35}Ti_{35}Cr_{10}Fe_{20-x}Mn_x$ (x = 6, 8, 10, 12, and 14) alloys. (f) XRD patterns of the Mn10 alloy at various state of hydrogenation in wt.%.

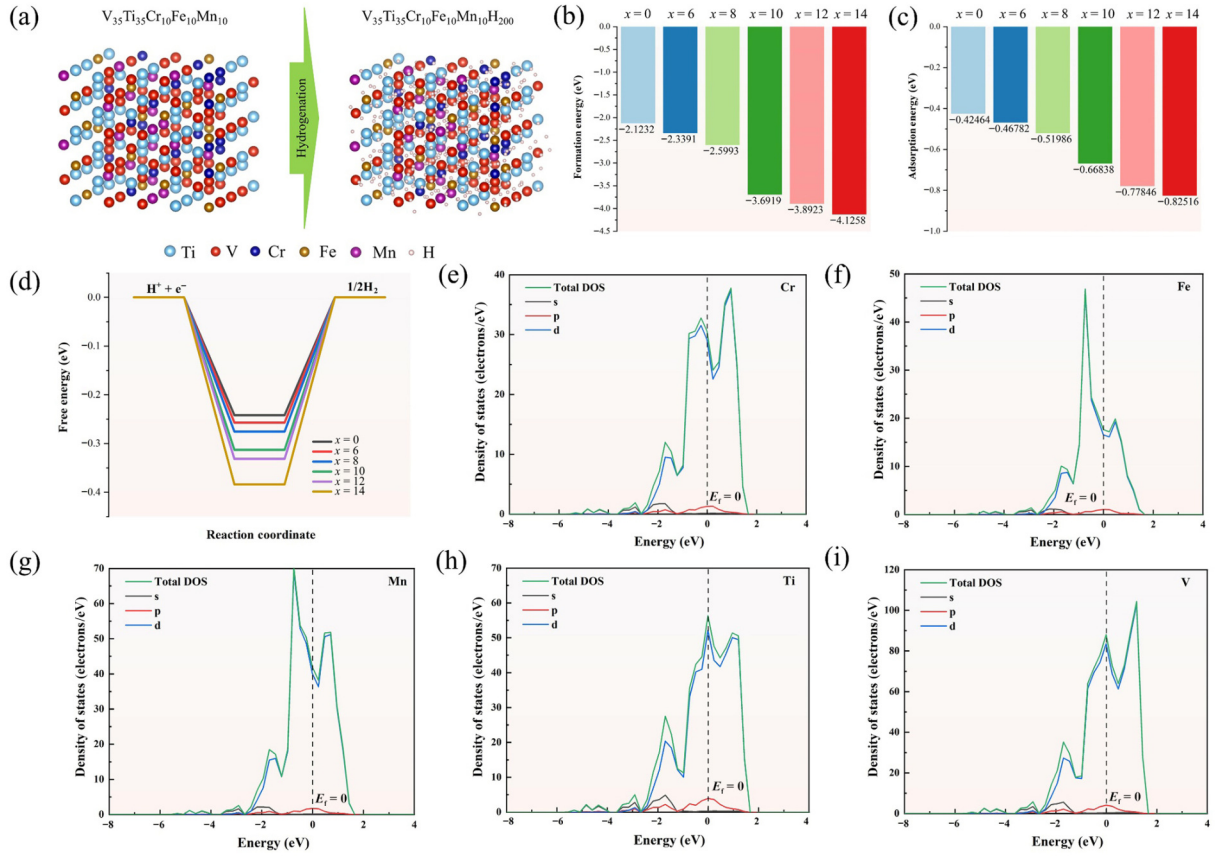

Figure 7 (a) One of SQS models of $V_{35}Ti_{35}Cr_{10}Fe_{20-x}Mn_x$ (x = 0, 6, 8, 10, 12, and 14) HEAs and corresponding hydride $V_{35}Ti_{35}Cr_{10}Fe_{10}Mn_{10}H_{200}$ (visualized using VESTA). (b) The formation energies of the HEAs. (c) The adsorption energies for the HEAs. (d) Calculated free-energy diagram for hydrogen release in different HEAs's hydride. (e)–(i) The total and partial density of states (DOS) for $V_{35}Ti_{35}Cr_{10}Fe_6Mn_{14}$ alloys, and the Fermi level is set at zero energy and marked by the vertical dotted lines.

the VEC of the alloys are less than 6.376% and 5.29, respectively, which all reside within the range, indicating the formation of the BCC solution solid. Here, it is seen that the formation energies of the $V_{35}Ti_{35}Cr_{10}Fe_{20-x}Mn_x$ (x = 0, 6, 8, 10, 12, and 14) alloys become significantly more negative as the amount of Mn substituted for Fe increases. It suggests that Mn substitution for Fe leads to relatively easier formation of BCC structural phases in high-entropy alloys. This is in perfect agreement with the results of XRD as well as SEM analysis.

Adsorption energy is the energy that is released when molecules or atoms are adsorbed into the medium during the adsorption process. It is a measure of the level of difficulty in the adsorption of substances. Figure 7(c) shows the adsorption energies for the alloys. All calculated adsorption energies are negative, suggesting that H atoms can be adsorbed stably in bulk and release heat, resulting in strong chemical adsorption. From the calculated results, it can be seen that the absolute value of adsorption energy increases gradually with the increase of the amount of Mn substituted Fe. This indicates that Mn substitution of Fe is easier to adsorb hydrogen and the formed hydride is more stable. This is in perfect agreement with the results of thermodynamic experiments.

Gibbs free energy (ΔG_H) is commonly used and widely accepted as a descriptor of the H desorption activity. To further investigate the hydrogen desorption properties of different alloy hydrides, we calculated the free energy of hydrogen of the HEAs. As shown in Fig. 7(d), the simulated free energies for $V_{35}Ti_{35}Cr_{10}Fe_{20}$, $V_{35}Ti_{35}Cr_{10}Fe_{14}Mn_6$, $V_{35}Ti_{35}Cr_{10}Fe_{12}Mn_8$, $V_{35}Ti_{35}Cr_{10}Fe_{10}Mn_{10}$, $V_{35}Ti_{35}Cr_{10}Fe_8Mn_{12}$, and $V_{35}Ti_{35}Cr_{10}Fe_6Mn_{14}$ were predicted to be −0.241, −0.257, −0.275, −0.312, −0.331, and −0.383 eV, respectively. It is clear that ΔG_H gets lower and lower with the increase of the amount of Mn substituted Fe, indicating that an increase in the concentration of Mn increases the binding strength of the system to H and decreases the escape of H_2.

The bond lengths between metal atoms and hydrogen atoms are closely related to the thermodynamics of hydrogen storage alloys. The bond lengths between H atom and the surrounding other atoms are listed in Table 4. It is shown that the bond lengths of all bonds are obviously shortened after Mn substituted Fe. It is well known that the bond length shortens and the bond energy increases. So, the dehydrogenation process needed more energy. This well elucidated the decrease of effective dehydrogenation rate of the HEAs at room temperature after the substitution of Mn for Fe.

In order to reveal underlying mechanism of hydrogen storage properties from the nature of the chemical bonding, the total density of states (DOS) and partial DOS (PDOS) for $V_{35}Ti_{35}Cr_{10}Fe_6Mn_{14}$ alloy were calculated, as shown in Figs. 7(e)–7(i), in which the Fermi level was set as zero in the x-axis. The calculated DOS for other alloy was shown in Figs. S1–S5 in the Electronic Supplementary Material (ESM). The calculated total DOS is dominated mainly by d states of V, Ti, Cr, Fe, and Mn. The results show that the substitution of Fe with Mn has a very weak effect on the PDOS of the other elements of the alloy, implying that the substitution of Fe with Mn mainly affects the electronic states of Fe and Mn without affecting the electronic properties of the other elements in the alloy on a large scale. As the amount of Mn

Table 4 Change of Bond lengths between H atom and surrounding atoms after hydrogen absorption in master alloy and Mn substituted alloys

Structures	V–H (Å)	Ti–H (Å)	Cr–H (Å)	Fe–H (Å)	Mn–H (Å)
$V_{35}Ti_{35}Cr_{10}Fe_{20}$	1.528	1.553	1.559	1.515	—
$V_{35}Ti_{35}Cr_{10}Fe_{14}Mn_6$	1.518	1.547	1.551	1.509	1.683
$V_{35}Ti_{35}Cr_{10}Fe_{12}Mn_8$	1.505	1.515	1.539	1.501	1.609
$V_{35}Ti_{35}Cr_{10}Fe_{10}Mn_{10}$	1.423	1.449	1.501	1.495	1.513
$V_{35}Ti_{35}Cr_{10}Fe_8Mn_{12}$	1.406	1.412	1.461	1.435	1.488
$V_{35}Ti_{35}Cr_{10}Fe_6Mn_{14}$	1.309	1.385	1.396	1.387	1.391

substitution increases, the peak of PDOS plots of Fe decreases and the peak of PDOS plots of Mn increases, suggesting that the hydrogenation capacity of the alloy may be enhanced as Mn substitutes for Fe. This is due to the fact that Mn may have better hydrogen adsorption capacity and higher electronic density of states compared to Fe, which would lead to an increase in the hydrogen adsorption capacity of the alloy. However, accordingly, if the Mn content is too high, it will affect the hydrogen release performance of the alloy and reduce its effective hydrogen storage capacity.

3.5 Cycling properties

The hydrogen uptake cycling characteristics of the five alloys at 298 K are shown in Figs. 8(a)–8(e), where a gradual decrease in hydrogen uptake is clearly observed with increasing cycling time. Mn6 maintained a capacity retention of 86.48% after 50 cycles, whereas that of Mn14 decreases to 67.46%. To investigate the reason for the capacity decay of the alloys, they were analyzed by XRD following the cycling experiments. As shown in Fig. 8(f), the five alloys were completely dehydrogenated after 50 cycles, and the XRD patterns corresponding to those of the pristine samples are shown in Fig. 1(a). This indicates that the phase composition of the alloys has good stability and that the formation of non-hydrogen-absorbing phases was prevented. Figure 9(a) shows the relationship between the main XRD peak full width at half maximum (FWHM) of the original sample and that post-cycling of the $V_{35}Ti_{35}Cr_{10}Fe_{20-x}Mn_x$ (x = 6, 8, 10, 12, and 14) alloys. From the relationship between the main peak FWHM of the sample post-cycling and the Mn content, a broadening of the peak after cycling, an overall broadening tendency of the alloy, and a reduction in peak intensity with increasing Mn content are evidenced. This indicates that the increase in the Mn/Fe ratio results in higher lattice shrinkage and expansion of the alloy during the hydrogen absorption and discharge cycle, thereby repeatedly causing the lattice deformation, distortion, and stress increase, which leads to a decrease in hydrogen capacity. Figures 9(b)–9(f) show the cyclic characterization diagram of $t_{0.9}$, which evidences that the hydrogen absorption rates of the five alloys maintain a steady state, although the saturated hydrogen absorption decreases with the increase of the number of cycles. This is mainly due to the uniform distribution of the different elements, solid solution structure, and synergistic effect between the elements, which together provide HEAs with a relatively smooth kinetic performance in the process of hydrogen adsorption.

3.6 Thermal conductivity properties

In practical applications, the use of hydrogen storage alloys must consider their thermal conductivity, because good thermal conductivity is the prerequisite for the alloy to be practically used in reactors such as hydrogen storage tanks. To this end, we further investigated the thermal conductivity properties of the high-entropy alloys. The laser flash method is a common and reliable means for measuring the thermal diffusivity (α), specific heat capacity (C_p), and thermal conductivity (λ) of materials. A short pulse laser is used to irradiate one surface of the test sample. The surface begins

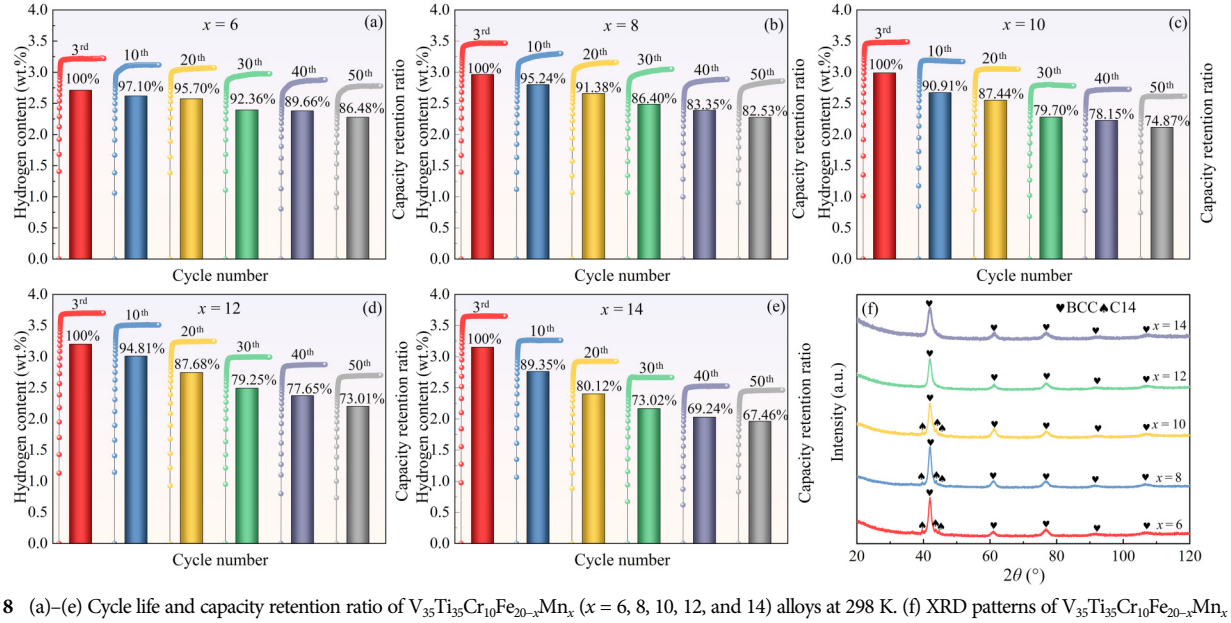

Figure 8 (a)–(e) Cycle life and capacity retention ratio of $V_{35}Ti_{35}Cr_{10}Fe_{20-x}Mn_x$ (x = 6, 8, 10, 12, and 14) alloys at 298 K. (f) XRD patterns of $V_{35}Ti_{35}Cr_{10}Fe_{20-x}Mn_x$ (x = 6, 8, 10, 12, and 14) alloys after 50 cycles.

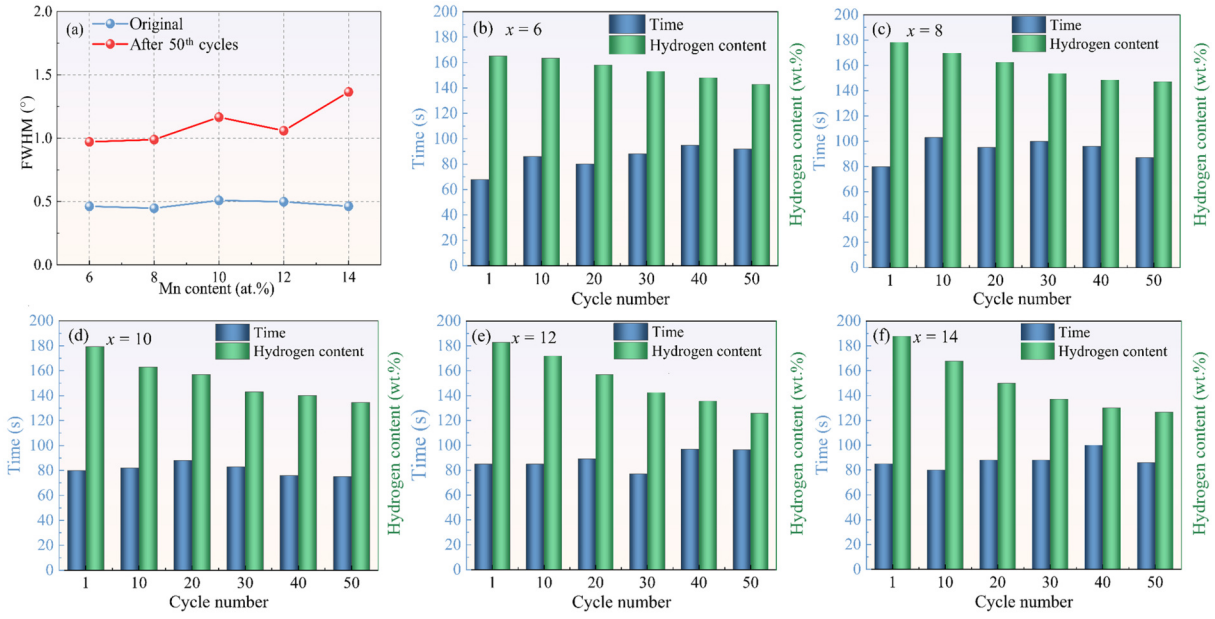

Figure 9 (a) FWHM of the main XRD peak before and after cycling as a function of the Mn content. (b)–(f) The cycling special figure of $t_{0.9}$.

to heat up after absorbing light, and a detector is used to monitor the time-varying rise in temperature on the backside surface. After the sample thickness has been obtained, α of the sample can be calculated by measuring the temperature rise as a function of time on the rear surface of the sample via Eq. (9) [62]

$$\alpha = 0.1388\frac{d^2}{t_{1/2}} \tag{9}$$

where α is the thermal diffusivity (mm²/s), d is the thickness of disc-like sample (mm), and $t_{1/2}$ is the time needed for the temperature of the back surface of the disc-like sample to reach one-half of its maximum value ΔT_{max} (s). By comparing the ΔT_{max} rises of the reference sample and test sample, the C_p of the test sample can be obtained via Eq. (10) [63]

$$C_p^{sample} = \left(\frac{\Delta T_{max}^{ref}}{\Delta T_{max}^{sample}} \cdot \left(\frac{m^{ref}}{m^{sample}}\right) \cdot C_p^{ref}\right) \tag{10}$$

where C_p^{sample} and C_p^{ref} are specific heat capacity of the test sample and reference sample (J/(g·K)), respectively; ΔT_{max}^{sample} and ΔT_{max}^{ref} are the maximum temperature rises of the test sample and reference sample (K), respectively; and m^{sample} and m^{ref} are the mass of the test sample and reference sample (g), respectively. The key characteristics of the reference graphite sample are listed in Table S1 in the ESM. After obtaining the thermal diffusivity, specific heat capacity, and density, the thermal conductivity can be calculated by the following equation [64]

$$\lambda = \rho \cdot C_p \cdot \alpha \tag{11}$$

where λ is the thermal conductivity (W/(m·K)), ρ is the density (g/cm³), C_p is the specific heat capacity of the test material (J/(g·K)).

Figure 10(a) shows the thermal diffusivity of the HEAs as a function of temperature over the temperature range of 25 to 100 °C. It can be clearly seen that the thermal diffusivity increases linearly with the increase of temperature. Figures 10(b) and 10(c) show the specific heat capacity and thermal conductivity of the alloys as a function of temperature. The specific heat capacity and thermal conductivity all gradually increases with increasing temperature. The alloy with the lowest Mn content has the highest thermal conductivity. The reason is that the thermal conductivity of elemental Mn at 20 °C is 7.82 W/(m·K), which is one order of magnitude lower than the thermal conductivity of elemental Fe at 20 °C, 80.2 W/(m·K). Figures 10(d) and 10(e) show the curves of thermal diffusion coefficient and thermal conductivity versus compacting pressure for Mn6 samples. It can be seen that the higher the molding pressure, the better the thermal conductivity of the disc-like sample. The studied high-entropy alloys all exhibit low thermal conductivity compared with pure V (40 W/(m·K) at RT [65]) or V-based alloys (12 W/(m·K) at RT [66, 67]). There are two main reasons for this. The first is that the disc-like sample tested is a sample that has been compacted from powder. The sample has pores inside, and its density is lower than that of the bulk alloys, so the thermal conductivity is relatively low according to Eq. (11). The second is that the thermal conductivity of a metal or alloy consists of two contributions: One is the free electron as a heat carrier, and the other is a phonon as a heat carrier. In high-entropy alloys, crystal defects such as high-density grain boundaries and severe lattice distortion in the solid solution formed by multi alloying elements scatter phonons and free electrons, resulting in restrictions on the their mean free path, leading to a decrease in thermal conductivity.

In addition to VEC being a good predictor of the structure of alloys, it is also important to investigate the relationship between thermophysical properties and VEC. Figure 10(f) shows the relationship between specific heat capacity and VEC. It can be clearly seen that the specific heat capacity of the samples first gradually increases and then gradually decreases as the VEC of the alloy increases. Figures 10(g)–10(i) show the variation curves of thermal diffusivity with VEC at different pressures. It can be seen that thermal diffusivity first decreases and then gradually increases with increasing VEC of the alloys. Figures 10(j)–10(l) show the variation curves of thermal conductivity with VEC and it can be seen that the thermal conductivity first decreases and then gradually increases with the increase in VEC. Based on the

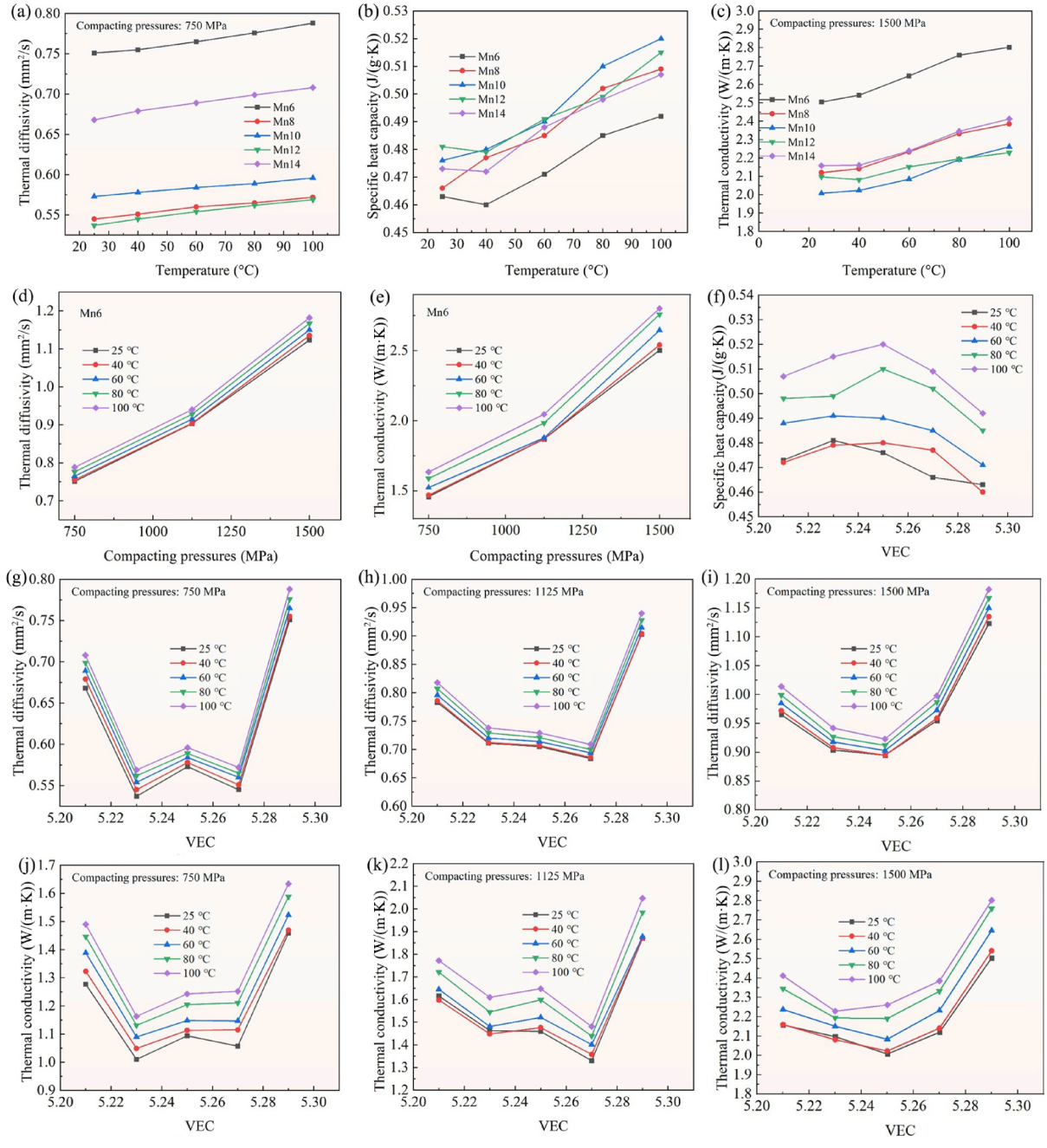

Figure 10 The relationships between (a) the thermal diffusivity, (b) specific heat capacity, and (c) thermal conductivity of the disc-like samples and sample temperatures. The relationships between (d) the thermal diffusivity and (e) specific heat capacity of the disc-like samples and compacting pressures. (f) The relationships between specific heat capacity of the disc-like samples and VEC. The relationships between thermal diffusivity of the disc-like samples and VEC under compacting pressures of (g) 750, (h) 1125, and (i) 1500 MPa. The relationships between thermal conductivity of the disc-like samples and VEC under compacting pressures of (j) 750, (k) 1125, and (l) 1500 MPa.

variation trends observed in Figs. 10(i) and 10(l), the critical VEC value for the HEAs system in this work is identified as 5.25. The thermal conductivity increases as the VEC deviates further from 5.25.

4 Conclusions

In this study, HEAs capable of storing hydrogen at room temperature were designed and prepared using empirical parameters. All alloys had nanocrystalline structures and the increase of Mn content resulted in the formation of alloys with a single-phase BCC structure that was more favorable for hydrogen absorption. The $V_{35}Ti_{35}Cr_{10}Fe_6Mn_{14}$ alloy achieved a hydrogen absorption of 3.79 wt.% at 298 K, which is higher than that of any of the hydrogen storage HEAs reported thus far. The designed alloys exhibited excellent activation and kinetic properties as they were fully activated following only one cycle of hydrogen absorption and discharge and were saturated with hydrogen within 100 s. The thermodynamic characterization of the alloys revealed that an increase in the Mn content increased the stability of the

hydride. Quasi-*in situ* XRD of the alloys revealed that they underwent a transition from BCC to pseudo-BCC to FCC structures during hydrogen absorption. Calculated by first-principles simulation, it is shown that the absolute value of adsorption energy increases gradually with the increase of the amount of Mn substituted Fe. This indicates that Mn substitution of Fe is easier to adsorb hydrogen and the formed hydride is more stable. This is also illustrated by the calculated bond lengths and Gibbs free energy. In addition, it was evidenced that the Mn content has a significant influence on the hydrogen-absorbing cycling performance of the HEAs, which are better for alloys with a lower Mn content, mainly due to the presence of the C14 phase. The cycling characteristics of $t_{0.9}$ were maintained in a stable state, which is mainly attributed to the homogeneous distribution of multiple elements, the solid-solution structure, and synergistic effects among the elements. The results of studies on the thermal conductivity of alloys have taught us that the VEC can be adjusted by appropriate compositional design to obtain the desired thermal conductivity. Therefore, HEAs suitable for room-temperature hydrogen absorption have been successfully developed and an in-depth study on the hydrogen absorption mechanism of these alloys have been conducted, providing new avenues for further research on solid-state hydrogen storage.

Electronic Supplementary Material: Supplementary material (DOS of alloys and key characteristics of the graphite sample) is available in the online version of this article at https://doi.org/10.26599/NR.2026.94908396.

Data availability

All data needed to support the conclusions in the paper are presented in the manuscript and the Electronic Supplementary Material. Additional data related to this paper may be requested from the corresponding author upon request.

Acknowledgment

This work was supported by the National Natural Science Foundation of China (Nos. 52474410, 52261041, and 51961032), the Fundamental Research Funds for Inner Mongolia University of Science & Technology (No. 2023QNJS119), the Natural Science Foundation of Inner Mongolia Autonomous Region of China (No. 2024ZD06), Major Scientific and Technological Projects in the Inner Mongolia Autonomous Region (No. 2025ZDSF0008), Science and Technology Development Plan of Jilin Province (No. 20240302001ZD), and Science and Technology Development Plan of Changchun (No. 2024GD01).

Declaration of competing interest

All the contributing authors report no conflict of interests in this work.

Author contribution statement

L. L.: Experimental design, data curation, project administration, funding acquisition, writing manuscript. K. C. Y.: Data curation, writing manuscript. L. P. C.: Project administration, validation. H. M. H.: Software, visualization. Y. D.: Experimental design, data curation, writing manuscript. B. B. C.: project administration. Y. C.: Resources, funding acquisition, project administration, validation. Y. Z. L.: Resources, funding acquisition. X. F. Z.: Resources, funding acquisition. All the authors have approved the final manuscript.

Use of AI statement

None.

References

[1] Le, T. T.; Sharma, P.; Bora, B. J.; Tran, V. D.; Truong, T. H.; Le, H. C.; Nguyen, P. Q. P. Fueling the future: A comprehensive review of hydrogen energy systems and their challenges. *Int. J. Hydrogen Energy* **2024**, *54*, 791–816.

[2] Zhuang, Z. C.; Wang, D. S. Advancing hydrogen energy through enzyme-mimetic electrocatalysis. *Front. Energy* **2025**, *19*, 563–567.

[3] Li, J. L.; Gan, T.; Yu, R. H.; Cai, J.; Zhuang, Z. C.; Zhu, H. Cooling crystallization at solid interfaces en route to a Janus nanocatalyst. *Adv. Mater.* **2026**, *38*, e12893.

[4] Yang, X. H.; Yang, J. R.; Zheng, X. B.; Dou, Y. H.; Li, H. T.; Zhang, Y.; Li, Y. F.; Wang, D. S.; Yu, B.; Zhuang, Z. C. Enzyme-mimetic single-atom catalyst design for green ammonia synthesis. *Adv. Energy Mater.* **2025**, *15*, 2501867.

[5] Qiao, W. F.; Yin, D. M.; Zhao, S. L.; Ding, N.; Liang, L.; Wang, C. L.; Wang, L. M.; He, M.; Cheng, Y. Effects of Cu doping on the hydrogen storage performance of Ti-Mn-based, AB_2-type alloys. *Chem. Eng. J.* **2023**, *465*, 142837.

[6] Lu, Z. Q.; Liu, H. Z.; Luo, H.; Wu, Z. Y.; Ning, H.; Fan, Y.; Wang, X. H.; Huang, X. T.; Huang, C. K.; Lan, Z. Q. et al. Effect of $Ti_{0.9}Zr_{0.1}Mn_{1.5}V_{0.3}$ alloy catalyst on hydrogen storage kinetics and cycling stability of magnesium hydride. *Chem. Eng. J.* **2024**, *479*, 147893.

[7] Emami, H.; Edalati, K.; Matsuda, J.; Akiba, E.; Horita, Z. Hydrogen storage performance of TiFe after processing by ball milling. *Acta Mater.* **2015**, *88*, 190–195.

[8] Hu, H. Z.; Xiao, H. Q.; Li, J.; Ma, C. M.; Yi, L. C.; Chen, Q. J. Hydrogen storage in Mo substituted low-V alloys treated by melt-spin process. *Chem. Eng. J.* **2023**, *455*, 140970.

[9] Qi, J. C.; Liang, Z. Q.; Xiao, X. Z.; Yao, Z. D.; Zhou, P. P.; Li, R. H.; Lv, L.; Zhang, X. Y.; Kou, H. Q.; Huang, X. et al. Effect of isostructural phase transition on cycling stability of ZrCo-based alloys for hydrogen isotopes storage. *Chem. Eng. J.* **2023**, *455*, 140571.

[10] Xiu, H. X.; Liu, W. Q.; Yin, D. M.; Ding, N.; Qiao, W. F.; Zhao, S. L.; Liang, L.; Liu, C.; Wang, S. H.; Wang, Q. S. et al. Multidimensional regulation of Ti-Zr-Cr-Mn hydrogen storage alloys via Y partial substitution. *Nano Res.* **2024**, *17*, 4211–4220.

[11] Yuan, Z. L.; Wang, Y. H.; Zhang, X. X.; Guan, S. Y.; Wang, X. J.; Ji, L. Q.; Peng, Q. M.; Han, S. M.; Fan, Y. P.; Liu, B. Z. Catalytic effects of V- and O-species derived from PrF_3/V_2C for efficient hydrogen storage in MgH_2. *Nano Res.* **2024**, *17*, 7117–7125.

[12] Liang, L.; Zhao, S. L.; Wang, C. L.; Yin, D. M.; Wang, S. H.; Wang, Q. S.; Liang, F.; Li, S. L.; Wang, L. M.; Cheng, Y. Heterojunction synergistic catalysis of MXene-supported PrF_3 nanosheets for the efficient hydrogen storage of AlH_3. *Nano Res.* **2023**, *16*, 9546–9552.

[13] Zhang, L. L.; Xiong, L.; Gao, B. Y.; Shi, Q. Y.; Wang, Y.; Han, Z. Y.; Zhang, Z. H.; Wang, C. L.; Wang, L. M.; Cheng, Y. Tuning microstructures of Mg-Ce-Ni hydrogen storage alloys via Cu and carbon nanotube additions. *Nano Res.* **2024**, *17*, 7203–7211.

[14] Yeh, J. W.; Chen, S. K.; Lin, S. J.; Gan, J. Y.; Chin, T. S.; Shun, T. T.; Tsau, C. H.; Chang, S. Y. Nanostructured high-entropy alloys with multiple principal elements: Novel alloy design concepts and outcomes. *Adv. Eng. Mater.* **2004**, *6*, 299–303.

[15] Tsai, M. H.; Yeh, J. W. High-entropy alloys: A critical review. *Mater. Res. Lett.* **2014**, *2*, 107–123.

[16] Cantor, B.; Chang, I. T. H.; Knight, P.; Vincent, A. J. B. Microstructural development in equiatomic multicomponent alloys. *Mater. Sci. Eng. A* **2004**, *375–377*, 213–218.
[17] Ren, P. F.; Gan, T.; Cai, J.; Hao, J. C.; Zhuang, Z. C.; Jin, C. Y.; Zhang, W. C.; Du, M. L.; Zhu, H. High-entropy environments enable metal surface-catalyzed nucleophilic electrooxidation. *Angew. Chem., Int. Ed.* **2025**, *64*, e202502776.
[18] Hao, J. C.; Wang, T. D.; Cai, J.; Gao, G. H.; Zhuang, Z. C.; Yu, R. H.; Wu, J. S.; Wu, G. M.; Lu, S. L.; Wang, X. F. et al. Suppression of structural heterogeneity in high-entropy intermetallics for electrocatalytic upgrading of waste plastics. *Angew. Chem., Int. Ed.* **2025**, *64*, e202419369.
[19] Hao, J. C.; Wang, T. D.; Yu, R. H.; Cai, J.; Gao, G. H.; Zhuang, Z. C.; Kang, Q.; Lu, S. L.; Liu, Z. H.; Wu, J. S. et al. Integrating few-atom layer metal on high-entropy alloys to catalyze nitrate reduction in tandem. *Nat. Commun.* **2024**, *15*, 9020.
[20] Kao, Y. F.; Chen, S. K.; Sheu, J. H.; Lin, J. T.; Lin, W. E.; Yeh, J. W.; Lin, S. J.; Liou, T. H.; Wang, C. W. Hydrogen storage properties of multi-principal-component $CoFeMnTi_xV_yZr_z$ alloys. *Int. J. Hydrogen Energy* **2010**, *35*, 9046–9059.
[21] Kunce, I.; Polanski, M.; Bystrzycki, J. Microstructure and hydrogen storage properties of a TiZrNbMoV high entropy alloy synthesized using laser engineered net shaping (LENS). *Int. J. Hydrogen Energy* **2014**, *39*, 9904–9910.
[22] Kunce, I.; Polański, M.; Czujko, T. Microstructures and hydrogen storage properties of La-Ni-Fe-V-Mn alloys. *Int. J. Hydrogen Energy* **2017**, *42*, 27154–27164.
[23] Kunce, I.; Polanski, M.; Bystrzycki, J. Structure and hydrogen storage properties of a high entropy ZrTiVCrFeNi alloy synthesized using laser engineered net shaping (LENS). *Int. J. Hydrogen Energy* **2013**, *38*, 12180–12189.
[24] Zlotea, C.; Bouzidi, A.; Montero, J.; Ek, G.; Sahlberg, M. Compositional effects on the hydrogen storage properties in a series of refractory high entropy alloys. *Front. Energy Res.* **2022**, *10*, 991447.
[25] Cermak, J.; Kral, L.; Roupcova, P. A new light-element multi-principal-elements alloy $AlMg_2TiZn$ and its potential for hydrogen storage. *Renew Energy* **2022**, *198*, 1186–1192.
[26] Cheng, B.; Dou, B.; Kong, L. J.; Wan, D.; Xue, Y. F. Synergistic and Competing Effects of Iron in TiVNbCr-Based High-Entropy Alloys for Reversible Hydrogen Storage, *Small*, **2025**, *21*, e08310.
[27] Park, K. B.; Park, J. Y.; Kim, Y. D.; Fadonougbo, J. O.; Kim, S.; Kim, H. K.; Kang, J. W.; Kang, H. S.; Park, H. K. Characterizations of hydrogen absorption and surface properties of $Ti_{0.2}Zr_{0.2}Nb_{0.2}V_{0.2}Cr_{0.17}Fe_{0.03}$ high entropy alloy with dual phases. *Met. Mater. Int.* **2022**, *28*, 565–571.
[28] Shen, H. H.; Hu, J. T.; Li, P. C.; Huang, G.; Zhang, J. W.; Zhang, J. C.; Mao, Y. W.; Xiao, H. Y.; Zhou, X. S.; Zu, X. T. et al. Compositional dependence of hydrogenation performance of Ti-Zr-Hf-Mo-Nb high-entropy alloys for hydrogen/tritium storage. *J. Mater. Sci. Technol.* **2020**, *55*, 116–125.
[29] Luo, L.; Han, H. M.; Feng, D. C.; Lv, W.; Chen, L. P.; Li, L. R.; Zhai, T. T.; Liu, S. X.; Sun, S. Y.; Li, Y. M. et al. Nanocrystalline high entropy alloys with ultrafast kinetics and high storage capacity for large-scale room-temperature-applicable hydrogen storage. *Renewables* **2024**, *2*, 138–149.
[30] Zhang, Y.; Zhou, Y. J.; Lin, J. P.; Chen, G. L.; Liaw, P. K. Solid-solution phase formation rules for multi-component alloys. *Adv. Eng. Mater.* **2008**, *10*, 534–538.
[31] Guo, S.; Ng, C.; Lu, J.; Liu, C. T. Effect of valence electron concentration on stability of fcc or bcc phase in high entropy alloys. *J. Appl. Phys.* **2011**, *109*, 103505.
[32] Yang, X.; Zhang, Y. Prediction of high-entropy stabilized solid-solution in multi-component alloys. *Mater. Chem. Phys.* **2012**, *132*, 233–238.
[33] Miracle, D. B.; Senkov, O. N. A critical review of high entropy alloys and related concepts. *Acta Mater.* **2017**, *122*, 448–511.
[34] Takeuchi, A.; Inoue, A. Classification of bulk metallic glasses by atomic size difference, heat of mixing and period of constituent elements and its application to characterization of the main alloying element. *Mater. Trans.* **2005**, *46*, 2817–2829.
[35] Perdew, J. P.; Burke, K.; Ernzerhof, M. Generalized gradient approximation made simple. *Phys. Rev. Lett.* **1996**, *77*, 3865–3868.
[36] Kresse, G.; Furthmüller, J. Efficient iterative schemes for *ab initio* total-energy calculations using a plane-wave basis set. *Phys. Rev. B* **1996**, *54*, 11169–11186.
[37] Kresse, G.; Joubert, D. From ultrasoft pseudopotentials to the projector augmented-wave method. *Phys. Rev. B* **1999**, *59*, 1758–1775.
[38] Blöchl, P. E. Projector augmented-wave method. *Phys. Rev. B* **1994**, *50*, 17953–17979.
[39] Grimme, S.; Antony, J.; Ehrlich, S.; Krieg, H. A consistent and accurate *ab initio* parametrization of density functional dispersion correction (DFT-D) for the 94 elements H–Pu. *J. Chem. Phys.* **2010**, *132*, 154104.
[40] Henkelman, G.; Uberuaga, B. P.; Jónsson, H. A climbing image nudged elastic band method for finding saddle points and minimum energy paths. *J. Chem. Phys.* **2000**, *113*, 9901–9904.
[41] Vegard, L. Die konstitution der mischkristalle und die raumfüllung der atome. *Z. Für Phys.* **1921**, *5*, 17–26.
[42] Monshi, A.; Foroughi, M. R.; Monshi, M. R. Modified scherrer equation to estimate more accurately nano-crystallite size using XRD. *World J. Nano Sci. Eng.* **2012**, *2*, 154–160.
[43] Liang, J.; Li, G. L.; Ding, X.; Li, Y.; Wen, Z.; Zhang, T.; Qu, Y. D. Effect of C14 Laves/BCC on microstructure and hydrogen storage properties of $(Ti_{32.5}V_{27.5}Zr_{7.5}Nb_{32.5})_{1-x}Fe_x$ (x = 0.03, 0.06, 0.09) high entropy hydrogen storage alloys. *J. Energy Storage* **2023**, *73*, 108852.
[44] Balcerzak, M. Structural, electrochemical and hydrogen sorption studies of nanocrystalline Ti-V-Co and Ti-V-Ni-Co alloys synthesized by mechanical alloying method. *J. Mater. Eng. Perform.* **2019**, *28*, 4838–4844.
[45] Hu, H. Z.; Ma, C. M.; Zhou, L.; Xiao, H. Q.; Chen, Q. J. Understanding crystal structure roles towards developing high-performance V-free BCC hydrogen storage alloys. *Int. J. Hydrogen Energy* **2022**, *47*, 25335–25346.
[46] Huang, Z. N.; Wang, Y. Q.; Wang, D.; Yang, F. S.; Wu, Z.; Wu, L.; Zhang, Z. X. Role of native defects and the effects of metal additives on the kinetics of magnesium borohydride. *Phys. Chem. Chem. Phys.* **2019**, *21*, 11226–11233.
[47] Ouyang, L. Z.; Liu, F.; Wang, H.; Liu, J. W.; Yang, X. S.; Sun, L. X.; Zhu, M. Magnesium-based hydrogen storage compounds: A review. *J. Alloys Compd.* **2020**, *832*, 154865.
[48] Li, Q.; Lu, Y. F.; Luo, Q.; Yang, X. H.; Yang, Y.; Tan, J.; Dong, Z. H.; Dang, J.; Li, J. B.; Chen, Y. et al. Thermodynamics and kinetics of hydriding and dehydriding reactions in Mg-based hydrogen storage materials. *J. Magnes. Alloys* **2021**, *9*, 1922–1941.
[49] Li, L. R.; Luo, L.; Chen, L. P.; Li, Y. M.; Liu, S. X.; Sun, S. Y.; Yang, F.; Li, Y. Z. Nanoscale microstructures and hydrogenation properties of an as-cast vanadium-based medium-entropy alloy. *Int. J. Hydrogen Energy* **2023**, *48*, 29230–29239.
[50] Qiao, Y. Q.; Du, C. C.; Tang, J. J.; Jia, P.; Zhang, X. Y.; Wang, J.; Ding, S. J.; Wen, Y. X.; Fan, C. Z.; Zhang, L. Q. et al. Micron-/nano-scale hierarchical structures and hydrogen storage mechanisms in a cast vanadium-based multicomponent alloy. *Nano Energy* **2021**, *90*, 106588.
[51] Floriano, R.; Zepon, G.; Edalati, K.; Fontana, G. L. B. G.; Mohammadi, A.; Ma, Z. L.; Li, H. W.; Contieri, R. J. Hydrogen storage in TiZrNbFeNi high entropy alloys, designed by thermodynamic calculations. *Int. J. Hydrogen Energy* **2020**, *45*, 33759–33770.
[52] Ma, X. F.; Ding, X.; Chen, R. R.; Cao, W. C.; Song, Q. Study on

hydrogen storage property of $(ZrTiVFe)_xAl_y$ high-entropy alloys by modifying Al content. *Int. J. Hydrogen Energy* **2022**, *47*, 8409–8418.

[53] Hu, J. T.; Zhang, J. J.; Xiao, H. Y.; Xie, L.; Sun, G. G.; Shen, H. H.; Li, P. C.; Zhang, J. W.; Zu, X. T. A first-principles study of hydrogen storage of high entropy alloy TiZrVMoNb. *Int. J. Hydrogen Energy* **2021**, *46*, 21050–21058.

[54] Hu, J. T.; Zhang, J. J.; Xiao, H. Y.; Xie, L.; Shen, H. H.; Li, P. C.; Zhang, J. W.; Gong, H. F.; Zu, X. T. A density functional theory study of the hydrogen absorption in high entropy alloy TiZrHfMoNb. *Inorg. Chem.* **2020**, *59*, 9774–9782.

[55] Nygård, M. M.; Ek, G.; Karlsson, D.; Sørby, M. H.; Sahlberg, M.; Hauback, B. C. Counting electrons-A new approach to tailor the hydrogen sorption properties of high-entropy alloys. *Acta Mater.* **2019**, *175*, 121–129.

[56] Ma, X. F.; Ding, X.; Chen, R. R.; Chen, X. G.; Song, Q.; Cui, H. Z. Study on microstructure and the hydrogen storage behavior of a TiVZrNbFe high-entropy alloy. *Intermetallics* **2023**, *157*, 107885.

[57] Luo, L.; Li, Y. M.; Yuan, Z. M.; Liu, S. X.; Singh, A.; Yang, F.; Li, B. Q.; Li, L. R.; Li, Y. Z. Nanoscale microstructures and novel hydrogen storage performance of as cast $V_{47}Fe_{11}Ti_{30}Cr_{10}RE_2$ (RE = La, Ce, Y, Sc) medium entropy alloys. *J. Alloys Compd.* **2022**, *913*, 165273.

[58] Zhang, C.; Song, A. N.; Yuan, Y.; Wu, Y.; Zhang, P. L.; Lu, Z. P.; Song, X. P. Study on the hydrogen storage properties of a TiZrNbTa high entropy alloy. *Int. J. Hydrogen Energy* **2020**, *45*, 5367–5374.

[59] Kumar, S.; Singh, P. K.; Kojima, Y.; Kain, V. Cyclic hydrogen storage properties of V-Ti-Cr-Al alloy. *Int. J. Hydrogen Energy* **2018**, *43*, 7096–7101.

[60] Floriano, R.; Zepon, G.; Edalati, K.; Fontana, G. L. B. G.; Mohammadi, A.; Ma, Z. L.; Li, H. W.; Contieri, R. J. Hydrogen storage properties of new A_3B_2-type TiZrNbCrFe high-entropy alloy. *Int. J. Hydrogen Energy* **2021**, *46*, 23757–23766.

[61] Sandrock, G. State-of-the-art review of hydrogen storage in reversible metal hydrides for military fuel cell applications. 1997.

[62] Czichos, H.; Saito, T.; Smith, L. E. *Springer Handbook of Metrology and Testing*. Berlin: Springer, 2011.

[63] Popilevsky, L.; Skripnyuk, V. M.; Beregovsky, M.; Sezen, M.; Amouyal, Y.; Rabkin, E. Hydrogen storage and thermal transport properties of pelletized porous Mg-2 wt.% multiwall carbon nanotubes and Mg-2 wt.% graphite composites. *Int. J. Hydrogen Energy* **2016**, *41*, 14461–14474.

[64] Min, S.; Blumm, J.; Lindemann, A. A new laser flash system for measurement of the thermophysical properties. *Thermochim. Acta* **2007**, *455*, 46–49.

[65] Jung, W. D.; Schmidt, F. A.; Danielson, G. C. Thermal conductivity of high-purity vanadium. *Phys. Rev. B* **1977**, *15*, 659–665.

[66] Klemens, P. G.; Williams, R. K. Thermal conductivity of metals and alloys. *Inter. Met. Rev.* **1986**, *31*, 197–215.

[67] Luo, L.; Han, H. M.; Chen, L. P.; Feng, D. C.; Li, L. R.; Zhai, T. T.; Chen, Z. W.; Gao, R. H.; Wu, H. B.; Liu, S. X. et al. Critical review of high-entropy alloys for catalysts: Design, synthesis, and applications. *Int. J. Hydrogen Energy* **2024**, *90*, 885–917.